

LETTERS

Uplift, thermal unrest and magma intrusion at Yellowstone caldera

Charles W. Wicks¹, Wayne Thatcher¹, Daniel Dzurisin² & Jerry Svarc¹

The Yellowstone caldera, in the western United States, formed ~640,000 years ago when an explosive eruption ejected ~1,000 km³ of material¹. It is the youngest of a series of large calderas that formed during sequential cataclysmic eruptions that began ~16 million years ago in eastern Oregon and northern Nevada. The Yellowstone caldera was largely buried by rhyolite lava flows during eruptions that occurred from ~150,000 to ~70,000 years ago¹. Since the last eruption, Yellowstone has remained restless, with high seismicity, continuing uplift/subsidence episodes with movements of ~70 cm historically² to several metres since the Pleistocene epoch³, and intense hydrothermal activity. Here we present observations of a new mode of surface deformation in Yellowstone, based on radar interferometry observations from the European Space Agency ERS-2 satellite. We infer that the observed pattern of uplift and subsidence results from variations in the movement of molten basalt into and out of the Yellowstone volcanic system.

In a previous satellite interferometric synthetic aperture radar (InSAR) study of Yellowstone⁴, interferograms from 1992 to 1997 revealed a change from caldera-wide subsidence that began in 1985 (ref. 5) to uplift that began in 1995 and by 1997 involved the whole caldera floor (Fig. 1) as well as the area of uplift shown in Fig. 2a. Because the area of uplift in Fig. 2a is under the north caldera rim, we refer to it as the NUA (north rim uplift anomaly). Surface movements from 1996 to 2002 have proven to be even more dynamic (Fig. 2), with important implications for the nature of the magmatic plumbing of Yellowstone caldera and large caldera systems in general. Campaign mode GPS measurements from 1995 to 2000 (ref. 6) first revealed that NUA had become an isolated area of uplift, in agreement with InSAR observations (Fig. 2) that are drawn from all available satellite radar data. As NUA continued to rise after 1995, vertical motion of the caldera floor connecting the two resurgent domes (Sour Creek, SC, and Mallard Lake, ML, in Fig. 1) changed from uplift to subsidence between late 1997 and early 1998. NUA continued to inflate as the caldera floor subsided until 2002 at which time both movements ceased, or at least paused (Fig. 2b–d).

In order to model a deformation source for the entire inflation episode at NUA, we formed the interferogram in Fig. 3a by summing the interferograms in Fig. 2a–c. The total amount of volume added by the modelled inflating sill beneath NUA (see Supplementary Information) shown in Fig. 3 is 0.06–0.1 km³. The best-fit model synthetic interferogram is shown in Fig. 3b and the residual is shown in Fig. 3c. In Fig. 3d we show a profile through Y–Y' (Fig. 3a) that passes through the peak uplift at NUA and the peak subsidence at SC. By all appearances, the uplift at NUA and the subsidence of the caldera floor are linked. Therefore, any model that explains the uplift should also explain the subsidence.

Past episodes of uplift and subsidence in the caldera have been

attributed to various combinations of the following two processes taking place beneath the caldera. (1) Pressurization and de-pressurization of an alternately self-sealed and leaking hydrothermal fluid reservoir that traps volatiles exsolved from a crystallizing rhyolitic magma⁷. (2) Movement, formation and crystallization of rhyolitic and/or basaltic magma.

Ingebritsen *et al.*⁸ noted that chloride flux measurements at Yellowstone—which provide a measure of the hydrothermal heat

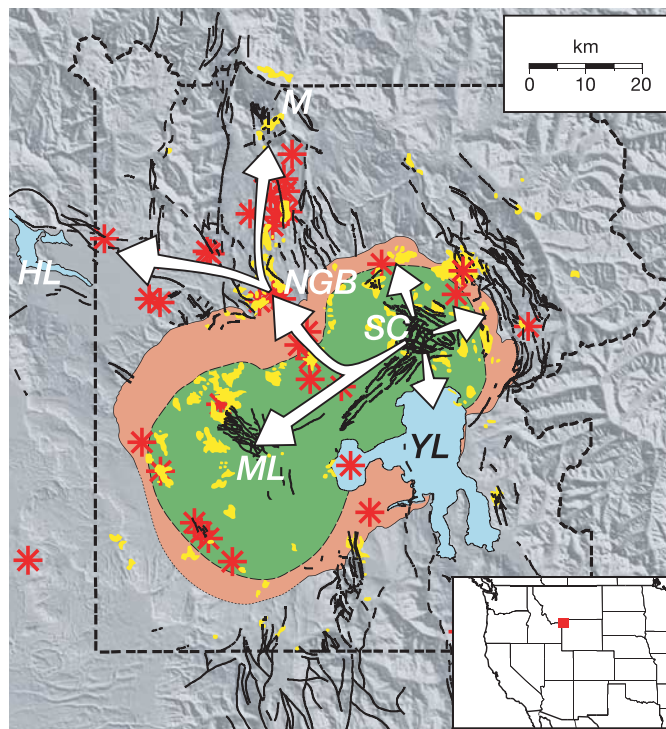


Figure 1 A map of structural, thermal and volcanic features in and around Yellowstone caldera. (Map taken from Christiansen¹.) The red symbols mark volcanic centres that erupted after the caldera-forming event 640 kyr ago. The areas of known past or present thermal activity are coloured yellow. The ring-fracture zone of the caldera is shown green, and the slumped zone between the ring-fracture zone and the best estimate of the caldera rim is shown salmon. The park boundary is the dashed black line. Faults active in the Quaternary are marked with black lines. The labelled features are Norris Geyser basin (NGB), Mammoth Hot Springs (M), Sour Creek dome (SC), Mallard Lake dome (ML), Hebggen Lake (HL) and Yellowstone Lake (YL). The white arrows show interpreted magma migration paths. The red square in the inset map (bottom right) shows the location of the study area.

¹US Geological Survey, MS 977, Menlo Park, California 94555, USA. ²US Geological Survey, David A. Johnston Cascades Volcano Observatory, 1300 SE Cardinal Court, Bldg 10, Suite 100, Vancouver, Washington 98683, USA.

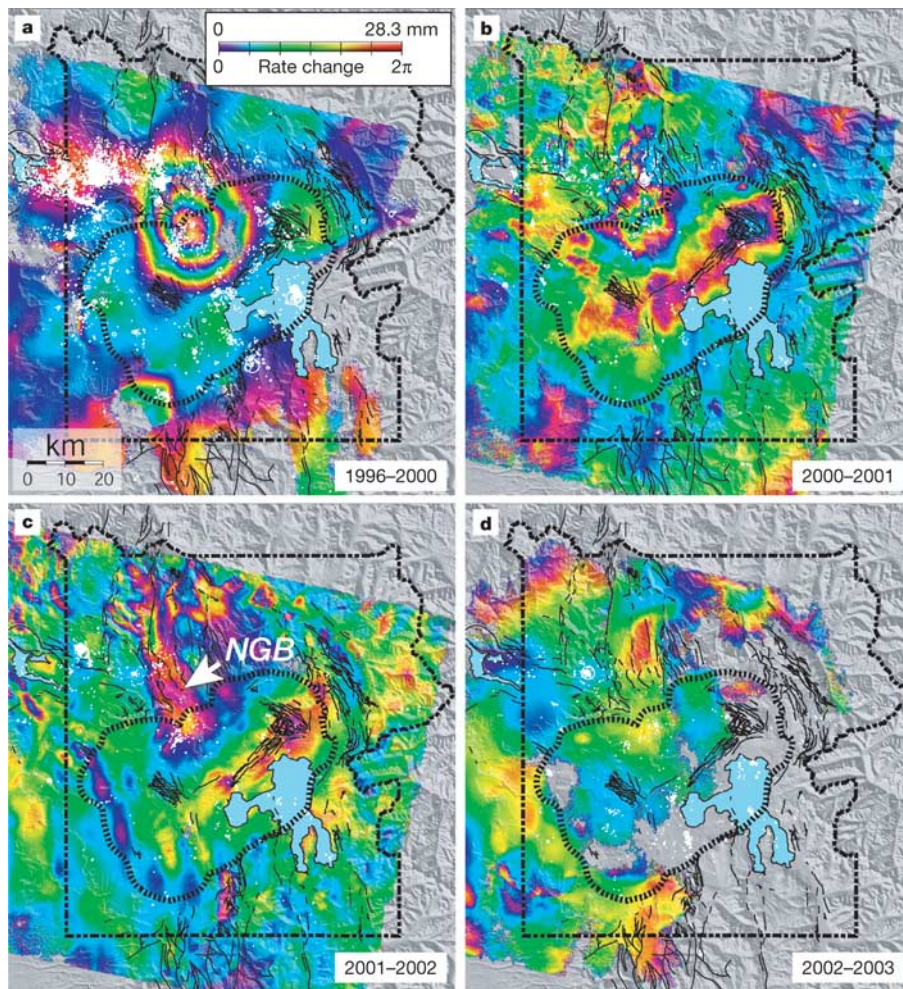


Figure 2 | Four interferograms showing the deformation during the episode of uplift at NUA. A colour change from violet to blue to green to yellow to red marks an increase in the range (distance from the satellite to points on the ground) of 28.3 mm. The white circles represent epicentres of earthquakes recorded during the time interval spanned by each interferogram. The interferograms have been generated using European Space Agency ERS-2 data (see Supplementary Information) and the two-pass method of interferometry²⁴. The extensive double dash length broken line in each panel shows the boundary of Yellowstone National Park. The short dash length broken line in each panel (within the park boundary) shows the approximate location of the 640,000-year-old caldera rim. **a**, Summer 1996 to summer 2000 interferogram. Although the caldera floor appears to have subsided only slightly, this period includes about 30 mm of caldera-wide uplift from 1996 to 1997 (ref. 4). Therefore, more than 30 mm of subsidence of the caldera floor occurred between the ML and SC resurgent domes (Fig. 1) from 1997 to 2000. **b**, Summer 2000 to summer 2001 interferogram. **c**, Summer 2001 to summer 2002 interferogram. The arrow labelled NGB marks the location of Norris Geyser basin. **d**, Summer 2002 to summer 2003 interferogram.

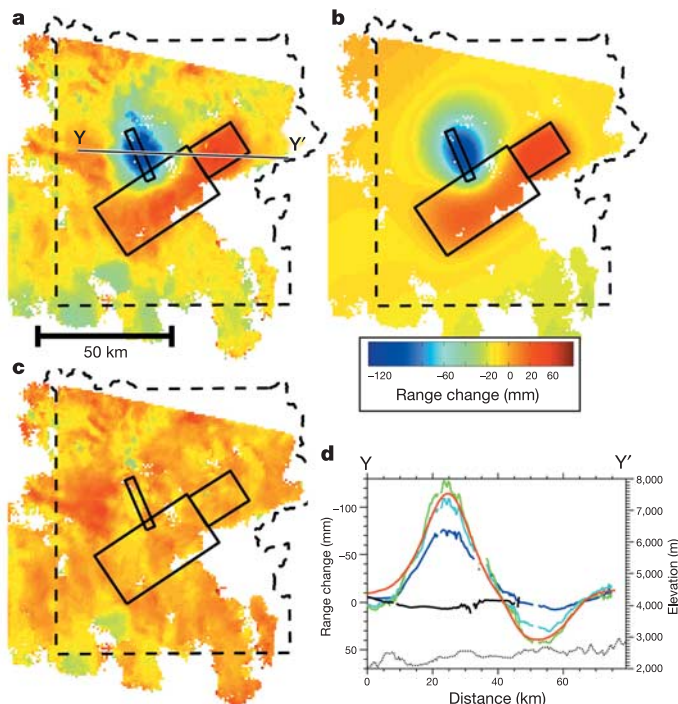


Figure 3 | Observed and modelled uplift at NUA and subsidence of the caldera floor. The black outlines are the surface projections of a north-northwest-trending expanding sill, and two northeast-trending contracting sills. The dashed line is the outline of Yellowstone National Park. **a**, A stacked interferogram formed by summing unwrapped versions of the interferograms in Fig. 2a–c. **b**, Synthetic interferogram from best-fit model. **c**, Residual interferogram formed by subtracting the synthetic interferogram (**b**) from the observed interferogram (**a**). **d**, Deformation profiles from Y to Y'. The colours denote: blue, 1996–2000 deformation; cyan, 1996–2001 deformation; green, 1996–2002 deformation; black, 2002–2003 deformation; and red, deformation from best-fit model (**b**). Elevation along the profile is shown by the black dotted line.

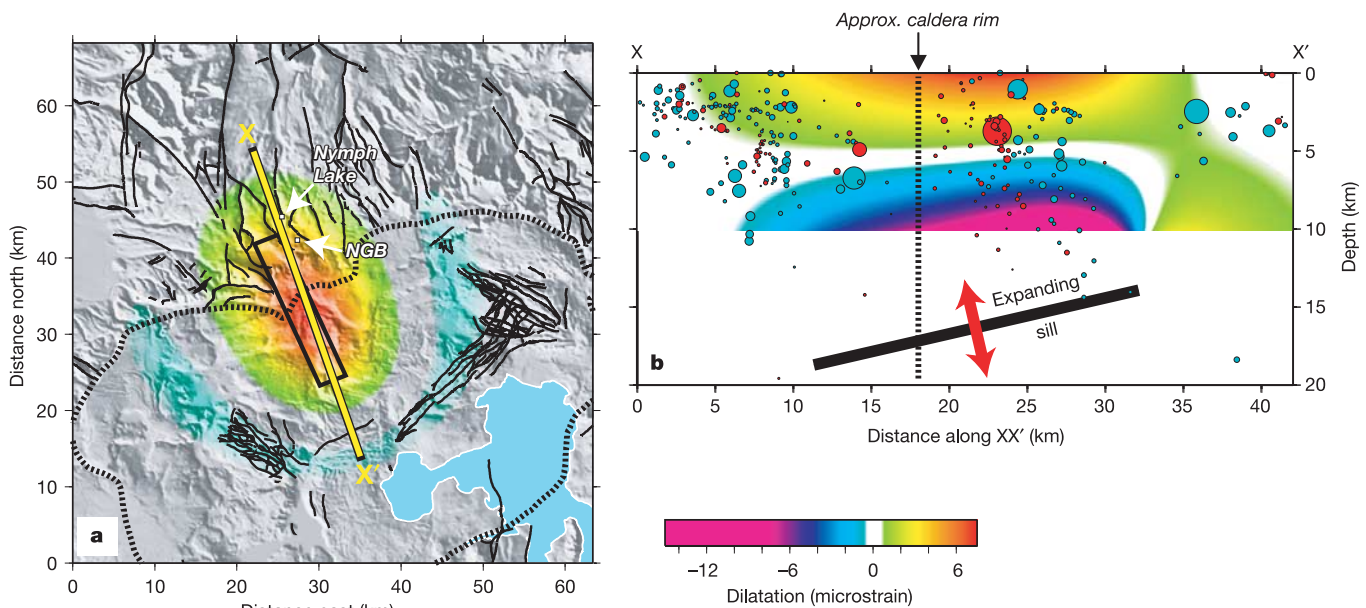


Figure 4 | Dilatation calculated from the inflating sill in Fig. 3. (Calculations were performed using Coulomb 2.5; ref. 25.) **a**, Dilatation at the surface resulting from the NUA uplift episode. The arrow labelled 'NGB' marks the location of Norris Geyser basin, and the arrow labelled 'Nymph Lake' marks the location of the newly formed line of fumaroles near Nymph Lake. The black lines are mapped faults active in the Quaternary¹. The black rectangle is the surface projection of the best-fit expanding sill. The broken line shows the approximate location of the 640,000-year-old caldera rim. **b**, Cross-section through X–X' in **a** resulting from the uplift episode. The peak dilatation is just under 7 microstrain at the surface. The cyan circles show

earthquakes greater than $M = 0.0$ that occurred before the uplift episode (1 January 1992 through to 31 December 1997) and the red circles show earthquakes greater than $M = 0.0$ that occurred during the uplift episode (1 January 1998 through to 13 August 2003). Earthquakes 10 km each side of the X–X' line are projected onto the cross-section. Size of circles is scaled to earthquake magnitude. Note that for better visualization, this scaling is different for the red and cyan circles; for two earthquakes with the same magnitude (one cyan, one red), the red circle plots at twice the diameter of the cyan circle.

loss—do not show any obvious temporal changes that might relate to changes in deformation style. This led them to suggest that deep magmatic processes were more likely causes of uplift/subsidence cycles at Yellowstone. Because chloride is one of the volatile species that is exsolved from rhyolitic magma during crystallization, any rupture of a sealed hydrothermal reservoir might be expected to eventually produce a corresponding increase in chloride flux at the surface. The lack of chloride flux anomalies that are correlated to deformation episodes does not rule out a hydrothermal deformation source, but it is more easily compatible with a magmatic source for deformation.

We propose that the observed patterns of uplift and subsidence result from variations in what may be nearly continuous movement of molten basalt in to and out of the Yellowstone volcanic system. Increases in the rate of basaltic magma flux into the caldera from beneath SC (Fig. 1) favour inflation of the caldera, whereas decreases favour subsidence. Increases in the rate of basaltic magma flux out of the caldera near NGB (Fig. 1) favour subsidence of the caldera, whereas decreases favour inflation. The main driving forces moving the basaltic magma into the system are the integrated buoyancy of the magma and the vertical gradient in normal stress. The combination of extensional stress (Yellowstone is at the northeastern corner of Basin-and-Range extension) and high heat flow present in Yellowstone is expected to favour emplacement of magma at rheological boundaries^{9,10}. If the flux of magma is too great, however, it would tend to continue its near vertical ascent¹¹.

We interpret the beginning of caldera uplift in 1995 as the introduction of a pulse of basaltic magma below SC from a source in the upper mantle. In the subsequent year, the uplift spread across the entire caldera⁴, including the area of NUA, as the magma spread horizontally at a rheological boundary. Previous studies have inferred the presence of a partially molten rhyolitic body^{1,12–14} that would form a rheological boundary with an accompanying sharp upward

decrease in density. As the basalt spreads beneath the caldera, it loses heat to the overlying rock. This heat keeps the geothermal system, and thus the surface hydrothermal features, active.

The basaltic magma escapes the caldera system at the three-way intersection of the northern caldera boundary, the west-northwest-striking seismic belt east of the Hebgen Lake fault zone, and the north-trending Norris–Mammoth corridor (Fig. 1). The seismic belt is a rift-like zone of north–south extension^{15,16} that is a site of minor post-caldera volcanism and extends west to the site of the 1959 M_s (surface wave magnitude) 7.5 Hebgen Lake earthquake. The Norris–Mammoth corridor is a zone of recurrent normal faulting, post-caldera volcanism, and active thermal features that extends north to beyond Mammoth Hot Springs¹.

Magma accumulated beneath the north caldera boundary, leading to continued uplift at NUA even as the larger part of the caldera floor subsided, because, in our interpretation, the outlet was unable to fully accommodate the increased flux of basaltic magma. The flux of magma out of the Yellowstone system is controlled by extra-caldera tectonic activity acting on fractured rock bordering the northern caldera boundary. Tectonic strain can either enhance or restrict the flow of magma out of the caldera. The two largest earthquake swarms recorded in Yellowstone each accompanied, or slightly preceded, the change from caldera-wide uplift to subsidence in 1985, and the change from caldera-wide subsidence to a brief episode of caldera-wide uplift in 1995 (refs 4, 17). A similar scenario has been suggested at Loihi volcano in Hawaii¹⁸, where a 1996 earthquake swarm was associated with magma chamber drainage, and a 2001 earthquake swarm was associated with magma chamber filling. The shallower southeastern end of the dipping sill that models the inflation at NUA is at the same depth as the two deflating sills it intersects beneath the caldera floor. The dipping sill deepens to the north-northwest by ~ 7 km at the proposed outlet, effectively forming a trap for the now negatively buoyant magma. Inclusion of GPS data⁶ in a joint

inversion of GPS and InSAR data (Supplementary Information) yields a similarly oriented prolate spheroid as an allowable model. Adoption of the spheroid does not change the proposed path of magma migration, but rather the mode of migration, to one more pipe-like in nature. As the magma leaves the caldera, it could become negatively buoyant by way of three separate processes: (1) cooling, (2) crystallization and (3) degassing of CO₂. The denser magma might then be emplaced in a large 10-km-thick sill inferred in ref. 19.

Inflation beneath NUA has led to extensive dilatation of the upper crust (Fig. 4). In faulted and fractured areas, such as geyser basins, this could lead to a dramatic increase in permeability. The 2000–2001 interferogram (Fig. 2b) shows several small (2–5 km) areas of inflation with ~30–50 mm of peak amplitude north of NUA in the highly faulted, thermally active Mammoth–Norris corridor, which may be atmospheric delay artefacts. However, drawing on the results of a study by Hanssen *et al.*²⁰ and ground-based radar (see Supplementary Information), it is more likely that these are areas of local inflation. These areas are also absent in the 1996–2000 interferogram (Fig. 2a), and they have broadened and extended northward in 2001–2002 (Fig. 2c) to occupy the entire Mammoth–Norris corridor. We suggest that the dilatation opened new or healed fractures or increased permeability in existing fractures, resulting in better communication between the shallow thermal systems and the deeper geothermal reservoir, thus forming the small-scale areas of inflation.

Thermal disturbances in Norris Geyser basin (Figs 1, 4) are near-annual events that have been related to yearly water table lows²¹. The thermal disturbances have recently become more pronounced (see Supplementary Information), perhaps in response to dilatation from NUA. Ingebritsen and Rojstaczer²² have demonstrated that the permeability of a geyser's fracture zone conduit may be an important factor in the eruption frequency of a geyser. Dilatation from NUA is thus a possible mechanism for increasing permeability in the geyser conduits, thereby increasing geyser eruption frequency. Husen *et al.*²³ noted an increase in geyser eruption frequency within hours after surface waves from the 2002 Denali earthquake produced ~0.5 microstrain of dynamic strain at Yellowstone. We calculate strains an order of magnitude greater (>6 microstrain) applied over a time interval four orders of magnitude longer (~3–4 yr). Inertial forces are insignificant for the dilatation we calculate, but there must be competition between (1) opening of cracks by hydro-fracturing and (2) healing of cracks through mineral precipitation and annealing that, beginning in 2000, led to the manifestation of shallow responses to the dilatation.

The episode of accentuated thermal unrest in the near-annual disturbances from 2000–2003 is not unique in the recorded history of Yellowstone National Park²¹. It is unique, however, that for this episode we have been able to use InSAR to track changes in the deformation field in the park during the unrest that suggest a cause-and-effect relationship. Indeed, past episodes of accentuated thermal unrest during near-annual disturbances in Norris Geyser basin may also have been caused by dilatation related to uplift from magma accumulation at depth, but in the absence of geodetic monitoring, earlier deformation episodes would have gone undetected.

Received 22 February; accepted 30 November 2005.

- Christiansen, R. L. The Quaternary and Pliocene Yellowstone plateau volcanic field of Wyoming, Idaho, and Montana. *US Geol. Surv. Prof. Pap.* **729-G**, 1–145 (2001).
- Pelton, J. R. & Smith, R. B. Recent crustal uplift in Yellowstone National Park. *Science* **206**, 1179–1182 (1979).
- Pierce, K. L., Cannon, K. P., Meyer, G. A., Trebesch, M. J. & Watts, R. D. Post-glacial inflation-deflation cycles, tilting, and faulting in the Yellowstone Caldera based on Yellowstone lake shorelines. *US Geol. Surv. Open-File Rep.* **02–0142** 1–62 (2002).

- Wicks, C., Thatcher, W. & Dzurisin, D. Migration of fluids beneath Yellowstone caldera inferred from satellite radar interferometry. *Science* **282**, 458–462 (1998).
- Dzurisin, D., Savage, J. C. & Fournier, R. O. Recent crustal subsidence at Yellowstone caldera, Wyoming. *Bull. Volcanol.* **52**, 247–270 (1990).
- Meertens, C. M., Smith, R. B. & Puskas, C. M. Crustal deformation of the Yellowstone caldera from campaign and continuous GPS surveys, 1987–2000. *Eos* **81**, V22F–19 (2000).
- Fournier, R. O. Hydrothermal processes related to movement of fluid from plastic into brittle rock in the magmatic-epithermal environment. *Econ. Geol.* **94**, 1193–1211 (1999).
- Ingebritsen, S. E. *et al.* Time-variation of hydrothermal discharge at selected sites in the western United States: implications for monitoring. *J. Volcanol. Geotherm. Res.* **111**, 1–23 (2001).
- Rubin, A. M. Propagation of magma-filled cracks. *Annu. Rev. Earth Planet. Sci.* **23**, 287–336 (1995).
- Watanabe, T., Koyaguchi, T. & Seno, T. Tectonic stress controls on ascent and emplacement of magmas. *J. Volcanol. Geotherm. Res.* **91**, 65–78 (1999).
- Dahm, T. Numerical simulations of the propagation path and the arrest of fluid-filled fractures in the Earth. *Geophys. J. Int.* **141**, 623–638 (2000).
- Eaton, G. P. *et al.* Magma beneath Yellowstone National Park. *Science* **188**, 787–796 (1975).
- Miller, D. S. & Smith, R. B. *P* and *S* velocity structure of the Yellowstone volcanic field from local earthquake and controlled source tomography. *J. Geophys. Res.* **104**, 15105–15121 (1999).
- Husen, S., Smith, R. B. & Waite, G. P. Evidence for gas and magmatic sources beneath the Yellowstone volcanic field from seismic tomographic imaging. *J. Volcanol. Geotherm. Res.* **131**, 397–410 (2004).
- Savage, J. C., Lisowski, M., Prescott, W. H. & Pitt, A. M. Deformation from 1973 to 1987 in the epicentral area of the 1959 Hebgen Lake, Montana, earthquake ($M_s = 7.5$). *J. Geophys. Res.* **98**, 2145–2153 (1993).
- Waite, G. P. & Smith, R. B. Seismotectonics and stress field of the Yellowstone volcanic plateau from earthquake first-motions and other indicators. *J. Geophys. Res.* **109**, doi:10.1029/2003JB002675 (2004).
- Waite, G. P. & Smith, R. B. Seismic evidence for fluid migration accompanying subsidence of the Yellowstone Caldera. *J. Geophys. Res.* **107**, doi:10.1029/2001JB000586 (2002).
- Wolfe, C. J., Okubo, P. G., Ekström, G., Nettles, M. & Shearer, P. M. Characteristics of deep (≥ 13 km) Hawaiian earthquakes and Hawaiian earthquakes west of 155.55°W. *Geochem. Geophys. Geosyst.* **5**, doi:10.1029/2003GC000618 (2004).
- Humphreys, E. D., Dueker, K. G., Schutt, D. L. & Smith, R. B. Beneath Yellowstone: Evaluating plume and nonplume models using teleseismic images of the upper mantle. *GSA Today* **10**, 1–7 (2000).
- Hanssen, R. F., Weckwerth, T. M., Zebker, H. A. & Klees, R. High-resolution water vapor mapping from interferometric radar measurements. *Science* **283**, 1297–1299 (1999).
- White, D. E., Hutchinson, R. A. & Keith, T. E. C. The geology and remarkable thermal activity of Norris Geyser Basin, Yellowstone National Park, Wyoming. *US Geol. Surv. Prof. Pap.* **1456**, 1–84 (1988).
- Ingebritsen, S. E. & Rojstaczer, S. A. Controls on geyser periodicity. *Science* **262**, 889–892 (1993).
- Husen, S., Taylor, R., Smith, R. B. & Heasler, H. Changes in geyser eruption behaviour and remotely triggered seismicity in Yellowstone National Park produced by the 2002 M 7.9 Denali fault earthquake, Alaska. *Geology* **32**, doi:10.1130/G20381.1 (2004).
- Massonnet, D. & Feigl, K. L. Radar interferometry and its application to changes in the Earth's surface. *Rev. Geophys.* **36**, 441–500 (1998).
- Toda, S., Stein, R. S., Reasenber, P. A. & Dieterich, J. H. Stress transferred by the $M_w = 6.9$ Kobe, Japan, shock: effect on aftershocks and future earthquake probabilities. *J. Geophys. Res.* **103**, 24543–24565 (1998).

Supplementary Information is linked to the online version of the paper at www.nature.com/nature.

Acknowledgements We thank R. Christiansen, S. Hurlwitz, J. Lowenstein, S. Ingebritsen, J. Savage and G. Waite for discussions, reviews and comments. European Space Agency (ESA) ERS-2 data were acquired through an ESA ENVISAT AO and through the WInSAR consortium (supported by NASA, NSF and the USGS). Help from K. Wendt and F. Boler with the GPS data is greatly appreciated. Collection of the GPS data, archived at UNAVCO, was funded by an NSF grant to R. Smith (Univ. of Utah).

Author Information Reprints and permissions information is available at npg.nature.com/reprintsandpermissions. The authors declare no competing financial interests. Correspondence and requests for materials should be addressed to C.W.W. (cwicks@usgs.gov).

Supplementary Information

Uplift, Thermal Unrest, and Magma Intrusion at Yellowstone Caldera, Observed with InSAR

Charles W. Wicks, Wayne Thatcher, Daniel Dzurisin & Jerry Svarc

Methods

The InSAR data (S-Table 1) were parsed before modelling using a quadtree algorithm^{S1,S2}. The parsed data points were used in an F-test to estimate 95% confidence limits. We modelled the NUA with three simple sources: a point source^{S3}, a prolate spheroid^{S4,S5}, and a dislocation model^{S6}. The depth to the centre of the best-fit model for each of the three sources was deeper than 11 km. The model that best-fit the InSAR uplift data is a single expanding sill (S-Table 2), located near the base of the seismogenic crust, that dips slightly to the NNW (manuscript Figs. 3, 4). A prolate spheroid in the same location (~13 km by 3 km, centred a little more than 11 km deep, plunging about 26° to the NW) also provided a good fit to the data (S-Table 2), however, an F-test revealed that the better fit provided by the sill was significant at more than 99%. The geometry of the expanding sill beneath NUA was determined by fitting the data in Fig. 2A. Estimated 95% confidence limits are: dip 7-34°, depth to the top of the sill 9-16 km, maximum width ~14 km, and maximum length ~29 km. The best-fit sill has preferred dimensions of ~3 by 23 km (Fig. 3). To mitigate trade-offs between the expanding sill source and the contracting sills used to fit the data in Fig. 3A, the geometry of the expanding sill was fixed to that of the best-fit model for the uplift data in Fig. 2A and only the amount of expansion was allowed to vary. Starting models for the contracting sills used to model the source of subsidence are the sills we previously (ref. 4) used to model caldera-wide subsidence from 1993 to 1995. The difference between the geometry and location of initial and final models of the contracting sills is not significant at the 95% level. The

depth to the contracting sills beneath the caldera floor is between 6 and 14 km. The overlap of the inflating sill at NUA and the deflating sill beneath the caldera (Fig. 3) is non-physical. An inflating sill with a smaller aspect ratio would be more appropriate here.

The expanding sill model provides a very good fit to the InSAR data at NUA, but a distributed source model could be constructed in the shallow crust consistent with a hydrothermal source of deformation, which would also fit the uplift data. However, the deformation signal at NUA does not appear to be affected by the discontinuity of the caldera rim. The smooth nature of the deformation signal (Figs. 2, 3) and the highly heterogeneous nature of the overlying crust (Fig. 1) argue for a deep source such as we have modelled. The distribution of hydrothermal areas (active in the past and present, Fig. 1) is discontinuous across the slumped zone of the caldera at NUA. Together with the lack of seismicity near the caldera rim in Figure 4B this suggests the absence of a continuous hydrothermal system across the NUA.

Orbit No. of Master Image	Date of Master Image	Doppler Centroid (Hz)	Orbit No. of Slave Image	Date of Slave Image	Doppler Centroid (Hz)	Perpendicular Component of Baseline (m)	Figure Number
7410	1996-09-19	142	28452	2000-09-28	2	31	2A
27951	2000-08-24	-321	33462	2001-09-13	-385	81	2B
32460	2001-07-05	-83	37971	2002-07-25	310	9	2C
38973	2002-10-03	637	43482	2003-08-14	652	293	2D

S-Table 1. ERS-2 data used in this study.

Source	Weighted RMS misfit (mm)	RMS misfit (mm)
Sill	0.0064	3.65
Prolate Spheroid	0.0073	4.46
Point Source	0.0094	6.63

S-Table 2. Root Mean Square (RMS) misfit for three simple sources used to model the NUA interferogram data in Fig. 2A.

To evaluate the robustness of the InSAR modelling results, we perform a joint inversion of GPS data collected during campaigns by the Univ. of Utah in 1995 and 2000 (ref. 6) and InSAR data spanning the time from 1995 to 2000 (S-Fig. 1). Access to the GPS data was gained through the UNAVCO archive and processed using GIPSY/OASIS II software^{S7} in an International Terrestrial Reference Frame 2000, North America fixed reference frame. The 1995-2000 interferogram is formed by stacking the 1996-2000 interferogram in Fig. 2C, and a 1995-1996 interferogram from Wicks et al.⁴ then parsed (S-Fig. 1) as the 1996-2000 interferogram was above.

To perform a joint inversion of the GPS data and the InSAR data, we use the following weighting scheme, developed by Simons et al.^{S8} and Fialko^{S9}, that is designed to balance the contribution between the two data sets. We normalize the GPS data (horizontal only, since the InSAR data provide better control on the vertical component of deformation than the GPS) and InSAR by applying a weighting vector with a sum of unity to the GPS and InSAR data sets.

$$\sum_{i=1}^N w_i = 1 \quad (1)$$

For the GPS data the individual weighting is:

$$w_i = \frac{1}{\sigma_i \sum_{j=1}^M \frac{1}{\sigma_j}} \quad (2)$$

where σ is the 95% confidence estimate for each measurement, and M is the number of horizontal measurements.

For the InSAR data the weighting vector is:

$$w_i = \frac{\sqrt{n_i}}{\sum_{j=1}^N \sqrt{n_j}} \quad (3)$$

where the weighting w_i is applied to sub-sampled point i , n_i is the number of points in the quad-tree cell from which the value for the point is derived, and n_j is the number of points in each of the N quad-tree cells.

The quantity that we are minimizing is then:

$$\sum_{i=1}^M [\alpha w_i (o_i - c_i)]^2 + \sum_{i=1}^N [w_i (o_i - c_i)]^2 \quad (4)$$

M is the number of horizontal GPS measurements and N is the number of InSAR measurements (quad-tree cells). The variable o is the observed value and c is the calculated value. The relative weighting factor α is set to one.

Using all the data shown in S-Fig. 1, the prolate spheroid source and dipping sill source still fit the data better, than a point source. Also note that in addition to the source parameters for each model, we have also inverted for a static shift parameter for the north component of GPS, the east component of GPS, and the InSAR data. With the inclusion of the GPS data, the dipping sill still fits the data better than the prolate spheroid, but the two are now indistinguishable at the 95% level. The dimensions of the best fit prolate spheroid are similar to that found in the InSAR modelling, but the favoured depth is shallower (~9 km depth) and the favoured plunge is nearly zero. The dimensions of the best-fit sill are within the 95% limits estimated for the best-fit sill model using the InSAR data alone, but two local minima are found with inclusion of the GPS data that are not

different from the narrow NW dipping sill model. One is a sill with an aspect ratio of two (length to width) that still dips shallowly to the NW, and the other is a long narrow sill that still has its long direction oriented to the NW, but dips shallowly ($\sim 5^\circ$) to the NE. In S-Figs. 1 and 2, we show comparisons between observations and calculations for the sill model that best fits the InSAR and GPS data (S-Fig. 1).

The eleven GPS stations most distal from the NUA (shown with dashed error ellipses, S-Fig. 1) are likely to be influenced by other deformation sources. We have marked measurements from the eleven distal GPS stations with red symbols and error bars in S-Fig. 2. Most of the outliers in S-Fig. 2 are red. If we exclude data from the eleven distal GPS stations in our inversion, the sill still fits the data slightly better than the prolate spheroid, but still with a difference that is insignificant at the 95% level. The main difference is that the best-fit sill model is now dipping shallower ($\sim 8^\circ$) and the sill length is over 30 km, slightly beyond the 95% interval found using only the InSAR data.

The main effect of adding the GPS data to the inversion is that the prolate spheroid source and narrow sill source are now found to be equally likely. This means that with this data we can not discern whether the mode of magma migration out of the caldera, as we have proposed, is sheet-like or pipe-like in nature.

Notes

In May 2000, Steamboat Geyser erupted after a 9-year period of inactivity. Steamboat Geyser, which has the distinction of being the geyser with the highest plume in the world (~ 100 m) has erupted five more times since. New thermal features have also formed, including a ~ 75 m line of fumaroles near Nymph Lake (Fig. 4). The near-annual disturbance in NGB was especially severe in the summer of 2003, with the eruption of Pork Chop geyser (active only as a hot spring after 1989), and near-boiling ground temperatures that led to closure of nearly half of the footpaths through NGB.

The small-scale areas of uplift in Fig. 2A are shown in higher resolution in S-Fig. 3. Drawing from the results of Hanssen et al.²⁰, the small-scale signals in the Norris-Mammoth corridor and the NUA for this interferogram are not likely to be a known source of “atmospheric effects”. The small spatial scale and high amplitude would most likely correspond to areas of precipitation (if they were atmospheric in origin)²⁰. The signals would not result from the presence of liquid water, but rather high water vapour content (resulting from partial evaporation of precipitation) beneath precipitating clouds²⁰. Radar reflectivity images from NEXRAD^{S10} (S-Fig. 4) show no precipitation in the entire Yellowstone area ten minutes before the data were acquired in each of the 2000 and 2001 images. Also note that the small-scale areas of uplift are only found in the areas of past or present hydrothermal activity (Fig. 1). Similar NEXRAD images from ~10 minutes before the acquisition time of data used in Fig. 2C (S-Table 1) also show no precipitation over Yellowstone, indicating the small scale large-amplitude anomalies in the Norris-Mammoth corridor in Fig. 2C are also not atmospheric in nature. Note also that the small-scale anomalies are restricted to the Norris-Mammoth corridor (Fig. 1, 2B, 3C; S-Fig. 3). The Norris-Mammoth corridor is a zone of recurrent faulting, where the only large excursion of post-caldera volcanism and hydrothermal activity takes place (Fig. 1). Of the ~40 Yellowstone interferograms spanning 1992 to 2003 we have examined, the 2000-2001 interferogram (Fig. 2B) is the only one with a string of small uplift-like features in the Norris-Mammoth corridor. This may just be coincidental, but we mention it because some may argue that the features could be caused by unusually prolific (perhaps unrealistically prolific) hydrothermal activity in the Norris-Mammoth corridor that produced localized water vapor or temperature variations.

The introduction of basaltic magma beneath the caldera could lead to rapid (even catastrophic) changes in the volcanic system. However, the presence of the partially molten rhyolitic body beneath Yellowstone would tend to stabilize associated thermal

effects. The heat of fusion for igneous rocks is over two orders of magnitude greater than the specific heat^{S11}. Therefore as long as the rhyolite body is partially molten, it serves as a thermal buffer that tends to stabilize the shallow part of the volcanic system against sudden changes in temperature (*e.g.*, during intrusion of basalt near the base of the rhyolite body).

Supplementary References:

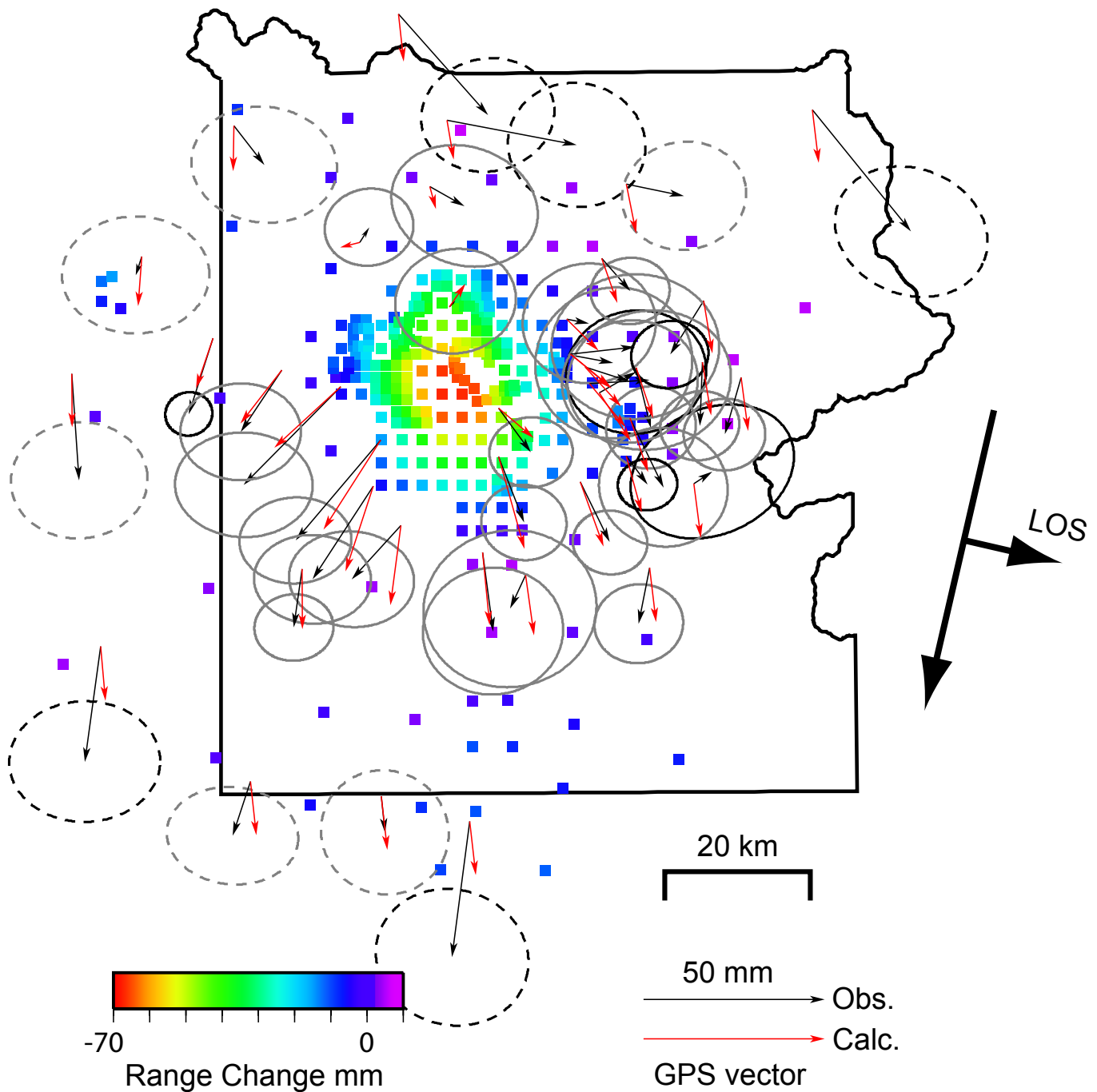
- S1. Jonsson, S., Zebker, H., Segall, P. & Amelung, F. Fault slip distribution of the 1999 Mw 7.1 Hector Mine, California earthquake, estimated from satellite radar and GPS measurements. *Bull. Seism. Soc. Am.* **92**, 1377-1389 (2002).
- S2. Simons, M., Fialko, Y. & Rivera, L. Coseismic deformation from the 1999 Mw 7.1 Hector Mine, California, earthquake, as inferred from InSAR and GPS observations. *Bull. Seism. Soc. Am.* **92**, 1390-1402 (2002).
- S3. Mogi, K. Relations between the eruptions of various volcanoes and the deformation of the ground surfaces around them. *Bull. Earthq. Res. Inst. U. Tokyo*, **36**, 99-134 (1958).
- S4. Yang, X.-M., Davis, P. M. & Dietrich, J. H. Deformation from inflation of a dipping finite prolate spheroid in an elastic half-space as a model for volcanic stressing. *J. Geophys. Res.*, **93**, 4249-4257 (1988).
- S5. Fialko, Y. & Simons, M. Deformation and seismicity in the Coso geothermal area, Inyo County, California: Observations and modeling using satellite radar interferometry. *J. Geophys. Res.*, 105, 21,781-21,794 (2000).
- S6. Okada, Y. Surface deformation due to shear and tensile faults in a half-space. *Bull. Seismol. Soc. Am.*, **75**, 1135-1154 (1985).
- S7. Webb, F. H., Zumberge, J. F. An introduction to GIPSY/OASIS-II, *JPL D-11088*, Jet Propul. Lab., Pasadena, Calif. (1995).

S8. Simons, M., Fialko, Y. & Rivera, L. Coseismic deformation from the 1999 Mw 7.1 Hector Mine, California, earthquake, as inferred from InSAR and GPS observations. *Bull. Seism. Soc. Am.*, **92**, 1390-1402 (2002).

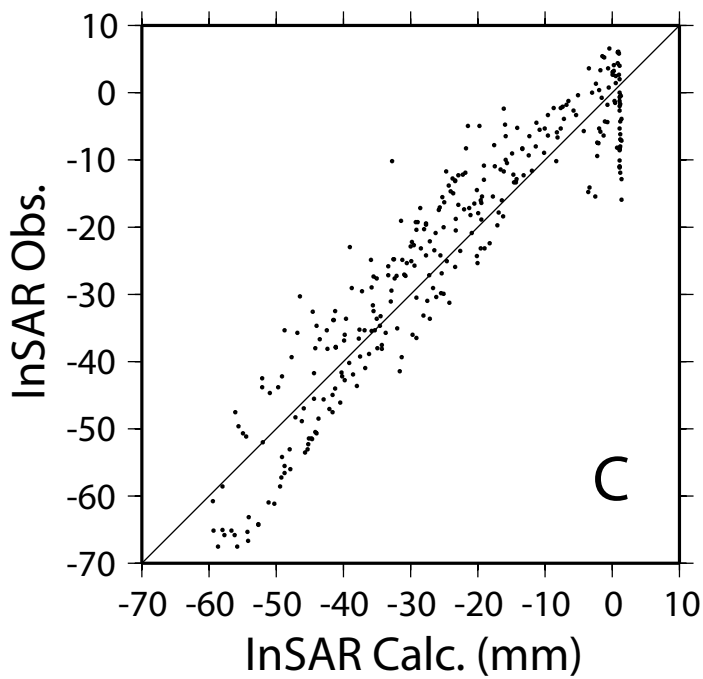
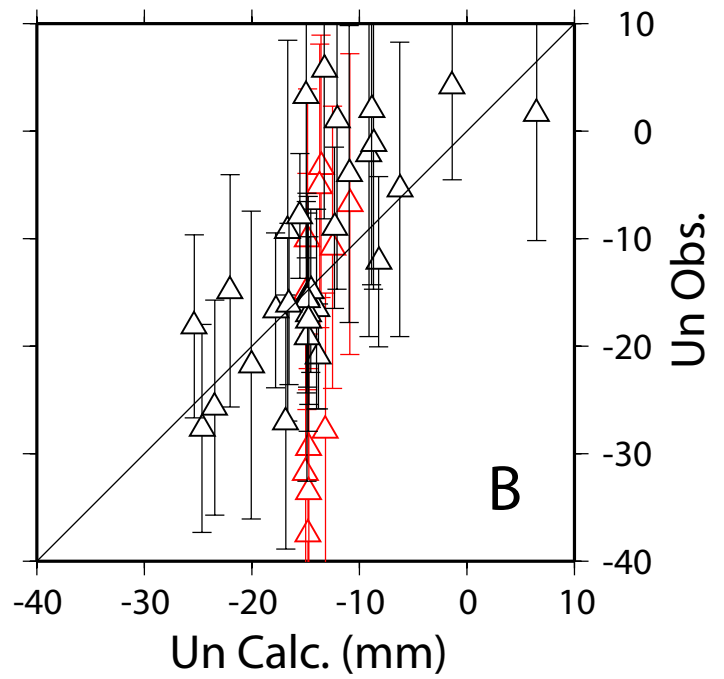
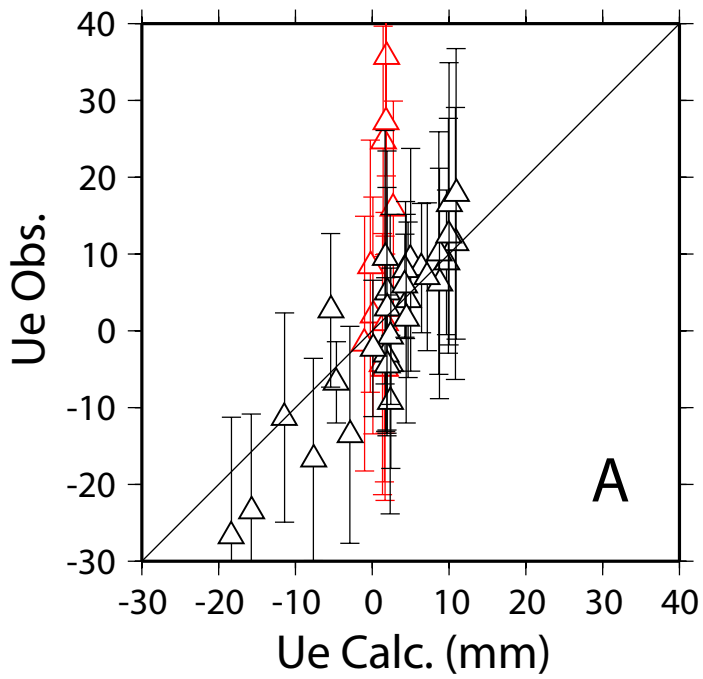
S9. Fialko, Y. Probing the mechanical properties of seismically active crust with space geodesy: Study of the co-seismic deformation due to the 1992 Mw7.3 Landers (southern California) earthquake. *J. Geophys. Res.*, **109**, doi:10.1029/2003JB002756 (2004).

S10. <http://www.ncdc.noaa.gov/oa/radar/radarresources.html>

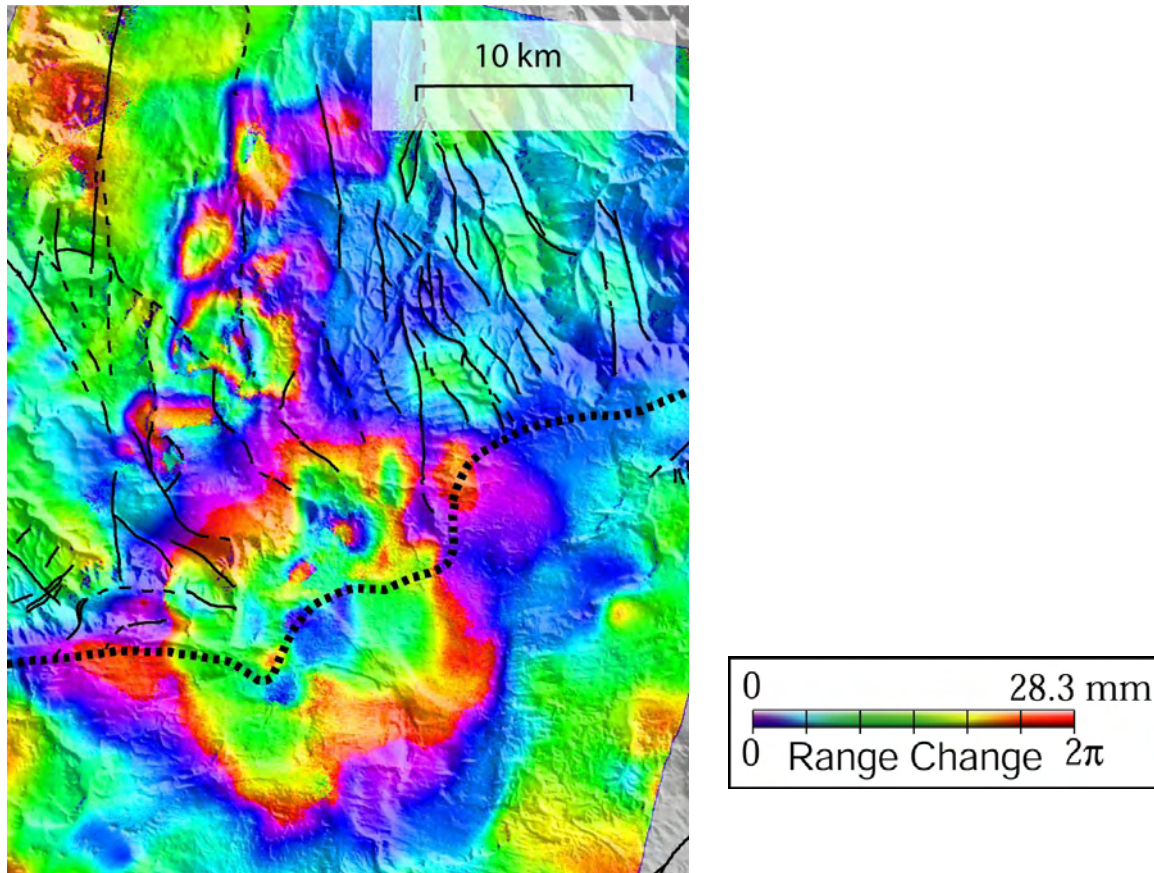
S11. Williams, H. & McBirney, A. R. *Volcanology*, Freeman Cooper and Co. San Francisco, California, USA (1979), p397.



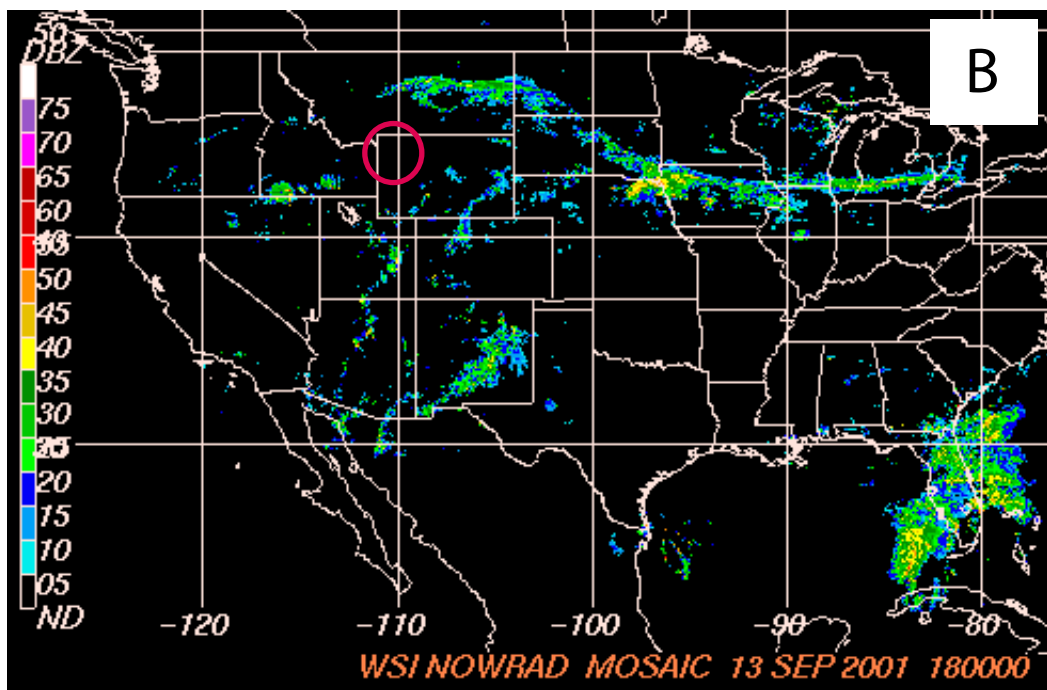
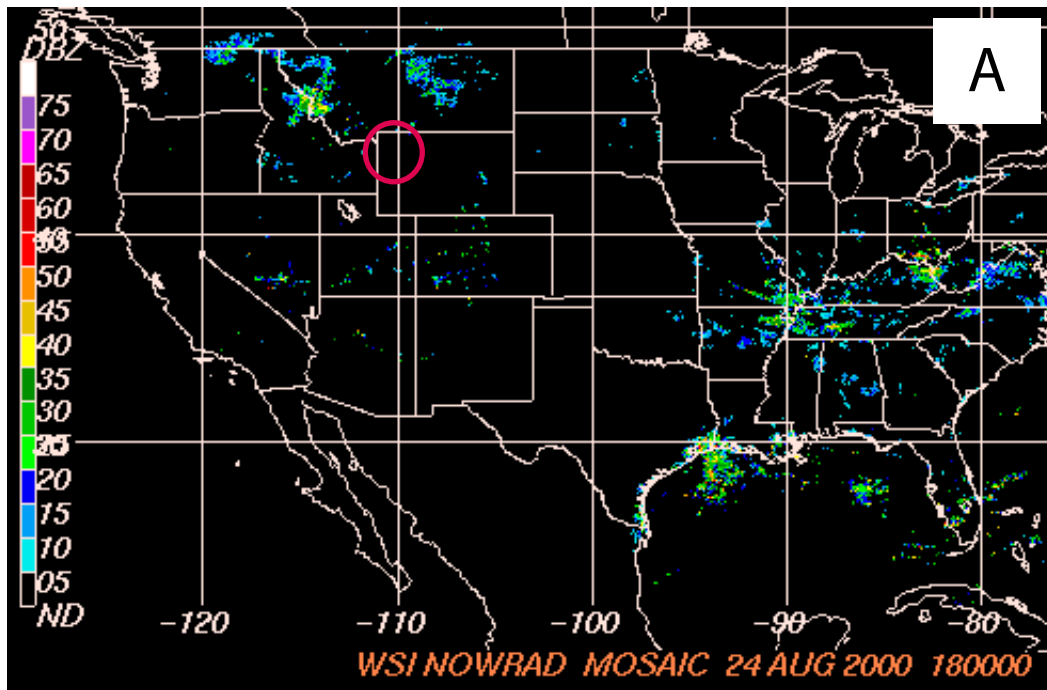
S-Figure 1. The colored squares are data parsed from an unwrapped interferogram formed by stacking the interferogram in Fig. 2A and an August 1995 to September 1996 interferogram used in Wicks et al.⁴. GPS vectors from Univ. of Utah GPS campaigns in 1995 and 2000 (ref. 6) are shown in black with 95% confidence ellipses. The red vectors show the calculated displacement from the model that best fits GPS and InSAR data (a long narrow sill). Black ellipses show where the calculated values do not fall within the 95% ellipses and gray ellipses show where the calculated values do fall within the 95% ellipses. The dashed ellipses are referred to in S-Fig. 2. The arrow labeled "LOS" shows the line-of-sight direction to the satellite, which is about 23 degrees from vertical in the center of the scene. The arrow perpendicular to the LOS vector shows the flight track of the satellite.



S-Figure 2. A comparison of the observed data and the calculated values for the best-fit sill model found from a joint inversion of the GPS and InSAR data. If the fit to the data was perfect, all points would fall on the diagonal lines. The red symbols and error bars in A and B correspond to the GPS stations with dashed ellipses in S-Fig. 1. **A.** The east-west component of GPS. **B.** The north-south component of GPS measurements. **C.** 1995-2000 InSAR data.



S-Figure 3. A high-resolution blow-up of the interferogram in Fig.2B .This better shows the uplift at NUA and the small-scale areas of uplift in the Norris Mammoth corridor. Faults active in the Quaternary are marked with Black lines and the approximate caldera rim is marked with a heavy black dashed line.



S-Figure 4. NEXRAD (Next Generation Weather Radar system) national mosaic radar reflectivity images⁵⁹. These two images are about 10 minutes before the ERS-2 data was acquired for the Master and Slave images used to calculate the interferogram from manuscript Fig. 2B and S-Fig. 1. They show areas of precipitation ranging from very light (light blue) to extreme (magenta to purple). The red circle surrounds Yellowstone and shows a lack of precipitation in each image. **A.** The image from ~10 minutes before the master image on Aug. 24, 2000. **B.** The image from ~10 minutes before the slave image on Sept. 13, 2001.